

Technical Articles

- Operation of FBTR at 30 MWt
- Design and Development of Diversified Real-Time Computer System for Future FBRs
- Fabrication of SiO₂ Microcantilevers using Direct Laser Writer and Wet Chemical Etching Methods

Young Officer's Forum

- High Temperature and Vacuum Tribological Properties of Ultrananocrystalline Diamond Thin Films

Young Researcher's Forum

- Alloy 617: The Avenue of Tomorrow's Advanced Ultra Supercritical Thermal Power Plant

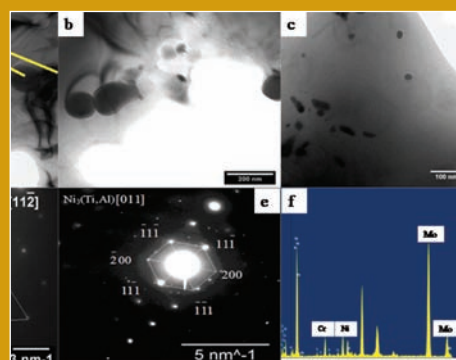
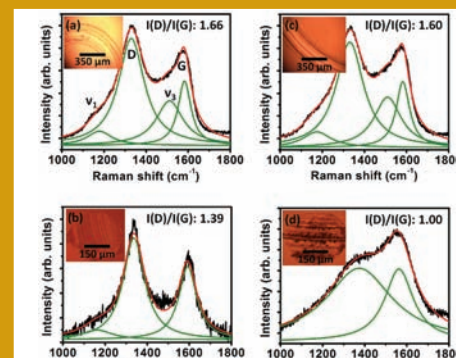
Forthcoming Meetings/Conferences

- The Second Quadrennial International CONFERENCE on Structural Integrity (ICONS-2018)
- 11th National Conference on REcent ADvances in Information Technology (READIT 2018)

News and Events

HBNI-IGCAR Corner

Awards & Honours



From the Editorial Committee

Dear Reader

It is our pleasant privilege to forward a copy of the latest issue of IGC Newsletter (Volume 116, April 2018 issue).

In the special technical article Shri K. V. Suresh Kumar and Colleagues from Reactor Facilities Group have shared their experience on Operation of FBTR at 30 MWt.

In the first technical article Shri M. Sakthivel and colleagues from Electronics & Instrumentation Group have shared their experience on Design and Development of Diversified Real-Time Computer System for future FBRs.

In the second technical article Dr. K. Prabakar and colleagues from Materials Science Group have discussed about Fabrication of SiO₂ microcantilevers using direct laser writer and wet chemical etching methods.

This issue's Young Officer's Forum features an article by Ms Revati Rani discussing about the High temperature and vacuum tribological properties of ultrananocrystalline diamond thin films.

Shri Aditya Narayan Singh has discussed on Alloy 617: The Avenue of tomorrow's Advanced Ultra Supercritical Thermal Power Plant in the Young Researcher's Forum.

We are happy to share with you the awards, honours and distinctions earned by our colleagues.

We look forward to your comments, continued guidance and support.

With best wishes and personal regards

Editorial Committee, IGC Newsletter

Operation of FBTR at 30.2 MWt

After installation of new steam generator module SGna 600B, secondary sodium west loop was filled in December 2017. Core changes for 26th irradiation campaign were completed in January 2018. At the end of 25th irradiation campaign, special subassembly IFZ 100 at the core centre and one Mark II fuel subassembly (SA) at 04/19 location attained their target burnup limits. Hence, these two subassemblies were transferred to periphery for in-pile cooling. The Mark I fuel subassemblies at 03/08 (125.4 GWd/t) and 03/10 (128.4 GWd/t) were shifted to 00/00 and 04/19 locations and two fresh Mark I subassemblies were loaded in their place. Two more fresh Mark I subassemblies were added for increasing the core reactivity. The core has 55 fuel subassemblies i.e. 43 Mark I + 4 Mark II + 8 MOX. Sodium flow measurements through the core subassemblies using Eddy Current Flow Meter and lifting force measurements for highly burnt subassemblies in the core were carried out. Reactor was started on 13th February and 26th irradiation campaign was initiated. The reactor power with the peak rated Mark I fuel subassembly at 01/02 operates at 400 W/cm is 30.2 MWt. The campaign ends when the Mark I subassembly at “00/00” location and Mark II at 04/11 attain the burnup limit of 140 GWD/t and 100 GWD/t respectively. The estimated heat transport parameters for the 26th irradiation campaign, respecting the limits on cold end ΔT of IHX & steam generator and stability of steam generator are given in Table 1. Table 2 details the reactor physics parameters for the campaign. Figure 1 gives the core configuration of 26th irradiation campaign.

It may be noted that the steam generators are capable of removing 35 MWt in the current configuration with three water tubes in each module blanked. The major missions of the 26th irradiation campaign are to continue irradiation of the sodium bonded metallic fuel pins (14.8%EU-6%Zr and 19%Pu-U-6%Zr) at locations in 1st ring (01/01 & 01/04) and natural U-6%Zr in 5th ring (05/13) and long term irradiation of structural materials. During

Parameter	Value
Reactor power / TG Power	30.2 MWt / ≈6.5 MWe
Reactor inlet/outlet temperature	380 /484 °C
SG inlet/outlet temperatures	481 /308 °C
Primary sodium loop flow	490.5 m ³ /h
Secondary sodium loop flow	276.5 m ³ /h
Feed water flow	50.09 m ³ /h
Feed water / steam temperature	190 / 455 °C
Steam pressure	121 kg/cm ²

Parameters	Value	Tech. Spec. Limit
Temp. Coefficient of reactivity	-4.26 pcm/°C	< -3.0 pcm/°C
Power Coefficient of reactivity	-7.22 pcm/MWt	< -4.0 pcm/MWt
Shut down margin (at 180°C)	5535 pcm	> 4200 pcm
Total CR worth	9540 pcm	-

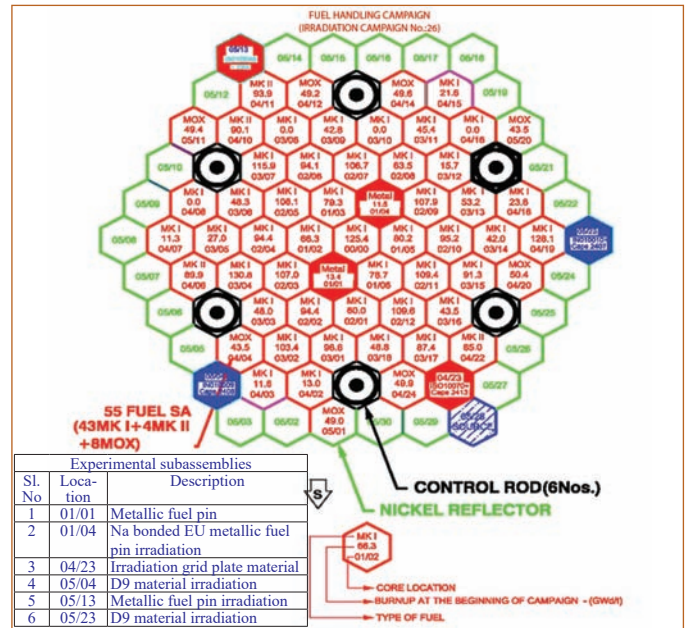


Figure 1: Core configuration for 26th irradiation campaign

the commencement of the campaign, reactor was operated at 25 kWt for reactor physics experiments and calibration of high range gamma detector Rrg 040. In order to check the high temperature performance of the newly replaced steam generator module SGna 600B, sodium temperature was raised to 400°C for observation for 15 days. Throughout this period reactor was operated at a low power of 25 kWt. Steam generator leak detection system was calibrated by actual injection of hydrogen in both the secondary sodium loops. Reactor was shut down on 2nd March 2018 for removal of high range gamma monitor and re-started on 5th March 2018. Power was raised gradually to 23 MWt and the steam generator safety valves were tested by TREVI test on 13th March. At 11:45 hours on 20th March, FBTR crossed a major milestone when reactor power was raised to the highest power level of 30.2 MWt. Dual channel digital automatic voltage regulator was commissioned by BHEL in FCR (Field Current Regulation) and PF (Power Factor) modes. Alternator was started in FCR mode; voltage was built up to 6.5 kV at a rate of 1.08 kV /minute and turbo generator was synchronized to grid in FCR mode. Turbine-generator (TG) was loaded up to 2.0 MWe in PF mode; performance was checked and found satisfactory. Subsequently TG was loaded up to 5.5 MWe. Thereafter the power to the grid was raised to 6.5 MWe. On 23rd March, reactor was shut down by manual LOR due to non-operability of CRDM #C. The defective motor of affected CRDM was replaced and the reactor was re-started at 03:00 hours on 25th March. On 29th March, power was again raised to 30.2 MWt and TG was synchronised to grid at a power of 6.5 MWe.

K. V. Suresh Kumar and Colleagues
Reactor Facilities Group

Design and Development of Diversified Real-Time Computer System for future FBRs

Indigenous design activities in the areas of nuclear instrumentation, monitoring and control electronics paved the way to self-reliance in the nuclear industry. The recent I&C systems developed for 500 MWe Prototype Fast Breeder Reactor (PFBR) is noteworthy. Fault-tolerant real-time computer (FT-RTC) systems are widely used to perform safe operation of nuclear power plants and safe shutdown in the event of any untoward situation. Design requirements for such systems need high reliability, availability, computational ability for measurements via sensors, control action via actuators, data communication and human interface via keyboard or display. All these attributes of FT-RTC systems are required to be implemented using best known methods such as redundant system design using diversified bus architecture to avoid common cause failure, fail-safe design to avoid unsafe failure and diagnostic features to validate system operation. In this context, the system designer must select efficient as well as highly reliable diversified bus architecture in order to realize on fault-tolerant system design.

System classification for reactor I&C

I&C systems provide protection, control, supervision and monitoring in nuclear power plants. Some of these functions are for safety critical, while others are safety related, and some functions which may have influence on industrial safety and availability but not directly related to nuclear safety are called non-nuclear safety system. In nuclear power plant, system and equipment are classified (or categorized) depending on their relationship to plant safety. In general, a graded classification approach is issued whereby the more direct relationship of a system to a safety function, the higher is its classification. This allows the systematic application of appropriate design and engineering techniques and just as importantly also helps to avoid over-design.

I&C design philosophy

I&C systems for nuclear power plant are mandated to undergo a rigorous verification process commensurate with the safety class of the system as specified in AERB safety guides D-10, D-20 and D-25. Effectiveness of common cause failure (CCF) is enhanced with channel and system independence. Performance requirement in terms of target reliability and availability are satisfied with redundant diverse system architecture. Requirements of fail-safe design, testability, maintainability and qualification of the systems specified in the standards for general I&C systems are applicable to computer based systems with some additional requirements detailed in D-25. The design requirements are assured by providing

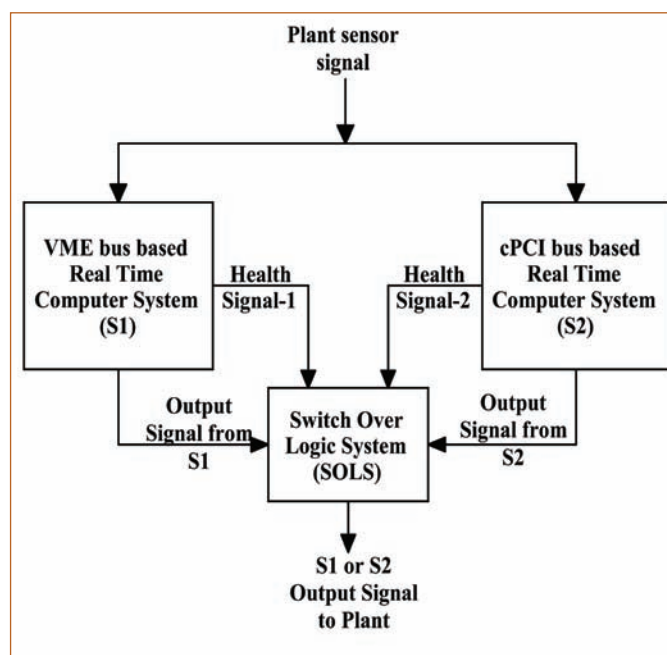


Figure 1: Fault tolerant system architecture with diversified RTC systems and SOLS

built-in test facility in every module. Software reliability is assured by following strict development life cycle process combined with zero-defect policy and is verified through V&V process.

Proposed fault tolerant RTC system architecture for FBRs

To handle large number of geographically distributed field signals in Nuclear Power Plant with high reliability and availability, two different backplane bus based RTC systems with Switch Over Logic System are proposed. This prevents system failure due to commonality between RTC systems as shown in Figure 1.

The use of diversified redundant system components or subsystems like Bus-Backplane, CPU & I/O Card, Power supply and Software development tools are important design strategies to mitigate risk in safety related applications in NPP. Redundant hardware reduces risk by multiplying the Mean-Time-Between-Failure (MTBF) value on two different hardware platforms like Versa Module Europa (VME) bus and compact Peripheral Component Interconnect (cPCI) bus. Using diversified hardware platform in "1-out-of-2" system (1oo2) architecture, the redundant capability is kept in the "hot standby" state. The Switch Over Logic System is highly reliable relay based (non-processor and non-software) system that checks the healthiness of both RTC systems. Depending on system healthiness, it routes healthy system's output to the plant. The state transition diagram of SOLS shown in

Figure 2 represents two online status of both RTC systems. During one RTC failure, switch over takes place in few milliseconds from present online system to hot-standby system thereby producing bumpless output to the final control element in the field. S1 Online corresponds to VME system & S2 Online corresponds to cPCI system enclosed in circles.

Online status indicates that the healthy system's output being routed to the plant. Depending on the RTC system's healthiness, SOLS changes its states as per the logic incorporated in the system. On system power-ON, SOLS starts from S1 Online state. Similarly, on system power off or failure of both systems, SOLS retains its last state and send fail safe output to the plant. The directed line connecting the circles indicates the transition between the states. The directed lines are labeled with an external cause of transition. The transition from one state to other state takes place only when the online system fails and the other system is in healthy condition. On manual selection, either system's output can be routed to the plant during maintenance. This type of system architecture helps in achieving redundancy with high availability by avoiding common cause failure. The ideal bus architecture for RTC system should also provide the required features in realizing above system architecture. Two standards have emerged as the dominant choices for such system bus, i.e. VME and cPCI. Both have similar physical and performance specifications along with support from numerous manufacturers that offer a range of processors, memory and peripherals. cPCI and VME bus technology can be used synergistically to achieve hardware/software redundancy to avoid common cause failure. Outwardly, they appear to be enough alike to compete for the same area of application, yet significant differences exists between these two bus specifications, fulfilling the diversified nature of their functionality suitable for our application.

Technological difference between cPCI& VME bus architecture to achieve diversification

Bus origin

VME bus was introduced by Motorola in 1981 and was designed as the I/O bus for 68000 CPU from Motorola. VME bus has commanded almost half of the embedded computer boards in the market. cPCI bus grew out of the personal computer's internal Peripheral Component Interconnect (PCI) bus. Because of its computer origins, the original PCI bus used edge connectors and had limited room for user defined I/O lines. In 1994, PCI Industrial Computer Manufacturers Group (PICMG) developed specifications that adapted PCI technology for use in industrial applications. PICMG first used personal computer's PCI/ISA form factor

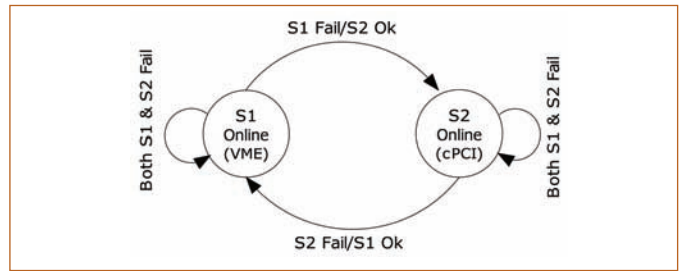


Figure 2: State transition diagram of fault tolerant RTC systems and SOLS. Online state indicates the RTC system's output being routed to the plant

(PICMG 1.x), then used PICMG 2.x which includes the definition of cPCI for Eurocard-based rack mount applications.

Functional Characteristics

cPCI was created to meld the low-cost components of the personal computer bus with the high-reliability of passive-backplane systems such as VME. Both cPCI and VME bus are processor-independent, high-performance buses in Eurocard physical form factor for the interconnection of high-bandwidth peripherals and intelligent controllers with the most powerful CPUs. Concurrent operations on the processor/memory bus and local bus can be realized. cPCI supports virtually all the processors available in the market, including Pentium, PowerPC, Sparc& Alpha. Since a large number of functions are available from the board-level manufacturer, any specific board can be designed rapidly according to the cPCI specification, including: communication, DSP & industrial I/O. Due to the broad support from the industry, the hardware design task is shortened using the cPCI bus. cPCI boards have several features like High density 2mm pin and socket connectors, Excellent vibration and shock protection characteristics, Shield for EMI/RFI protection, I/O connections on front or rear of backplane module and staged power pins for hot swapping that make them ideal for development of embedded systems for nuclear power plant. In cPCI I/O bus, one host interacts with multiple slaves whereas VME bus supports peer multiprocessing. Technology distinctions certainly exist between VME and cPCI bus. However, technical considerations are the only factors in designing diversified RTC systems in fault tolerant system design.

Synchronous Vs. asynchronous bus

The technical features that currently favor these buses are speed and passiveness of backplane. The data rate for both VME and cPCI are 60 and 100 MB/s respectively that suits most of the safety applications in NPP. Furthermore, cPCI provides a synchronous interface, whereas VME bus provides an asynchronous interface to its peripherals.



Figure 3: ARM9 Processor based CPU board



Figure 4: 30 Channel analog input board



Figure 5: 4 Channel analog output board

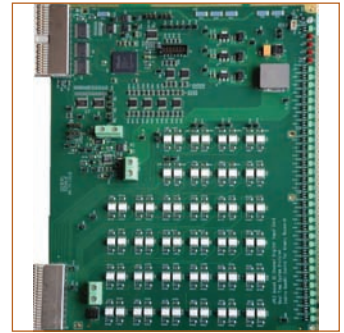


Figure 6: 32 Channel digital input board

Reflected wave versus incident wave switching

cPCI takes a radically different approach to bus termination. It eliminates the termination networks altogether and actually takes advantage of the reflected wave front. The bus driver is designed to drive the line about “halfway”, as the wave front propagates to the end of the line. When the wave front reaches the end of the bus, it is reflected back with doubled strength and the receiver switches as the wave front passes them second time in the other direction. VME takes the approach of “incident wave” thereby needing proper termination of all bus lines to prevent unwanted reflection. cPCI is based on CMOS, which means that steady state DC currents are minimal whereas VME is based on TTL thereby consuming more power. cPCI bus should maintain the minimum clock cycle time to 30ns at 33MHz. The maximum clock skews on the clock when measured on the clock pin of two cPCI components is 2ns. The minimum clock slew rate is 1V/ns and maximum slew rate is 4V/ns. The clock frequency can be changed as long as the clock edges remain clean and the minimum clock period for clock high time and clock low time are not violated.

Bus arbitration

When cPCI bus master requires using the bus, it must request the bus from the cPCI bus arbiter. The cPCI specification defines the timing of the request and grant handshaking, but not the procedure used to determine the winner of a competition. The algorithm used by cPCI bus arbiter to decide which of the requesting bus masters will be granted use of the cPCI bus is system specific, whereas VME bus with single master, asks for the bus, gets it and keeps it. Two or more masters in VME can request the bus at the same time on the same request level, and then proximity to slot one is used to determine who will get the bus. Arbitration is done by the system controller that resides in slot 1. Rear I/O Modules

cPCI offers rear I/O capability, which allows connection of all the cables on the back of the chassis. The cables include: communication signals, sensors & actuators. Since swapping

an adapter no longer requires disconnecting all the signals, this reduces the cost of wiring and maintenance time. This feature is also available in some versions of the 6U VME bus standard. However, cPCI offers more free pins in terms of I/O connections in 6U format compared to VME bus.

Hot-pluggability

A key performance element of RTC systems is their response to interrupts and Hot-Pluggability. This feature helps in reducing system down-time while the other standby system is still in operation. In nuclear power plant, this feature becomes handy not for online system but also for systems that have reported error, malfunctions or meant for maintenance. cPCI system has four physical Interrupt Request (IRQ) lines and assigns the IRQ numbers during hot-plug initialization process and prevents interrupt conflicts. Whereas VME64x also support a hot-plug operation and the interrupt structure is simpler than cPCI's since each of the interrupting devices has a vector number that the system designer pre-assigns. This vector number is unique to the interrupting device, eliminating the chance of having conflicts. The weakness of VME system is that system configuration, resource assignment and avoiding conflict is the developer's responsibility and design documents must be thorough and accurate to support future addition or change to the system in later stage of development.

Design of cPCI bus based RTC system

Towards the development of the system, a CPU card based on an ARM-9 processor and a set of Input/output (I/O) cards were developed. All the I/O cards support hot-swap and geographic addressing capability. In order to mitigate the component obsolescence problem, the 32 bit PCI target controller and associated glue logic for the I/O cards were indigenously developed using VHDL. U-boot was selected as the boot loader and arm Linux 2.6 as the preliminary operating system for the CPU card. Board specific initialization code for the CPU card was written in ARM assembly language and serial port initialization was written in 'C'



Figure 7: 32 Channel digital output board



Figure 8: 16 Channel relay output board



Figure 11: 4/12/4 Channel counter timer board



Figure 12: 16 Channel leak detector board

language. Boot loader along with Linux 2.6 kernel and 'jffs2' file system was flashed into the CPU card. Test application software written in 'C' language was used to test the various peripherals of the CPU card. Device driver for the I/O cards were developed as Linux kernel modules and application library was also developed. Environmental and EMI/EMC pre-qualification testing of the system were completed.

CPU board

ARM based SoC contains a rich set of peripheral controllers like PCI controller, gigabit Ethernet MAC, memory controllers for DDR, SRAM and flash, dual USB controllers, four UARTs has been used in the board.. This reduces the external component count, making board layout simple. Processor core operates at various clock frequencies of 250MHz, 200MHz and 125MHz, which can be selected by programming an internal register. An external 25MHz crystal is provided to give the reference clock to the SoC. Linux kernel along with jffs2 file system is found to be around 4 MB. Hence, an 8MB NOR flash is chosen for storing the boot program, thereby giving enough space for user applications and future kernel enhancements. DDR memory of 64MB is provided and organized as two 16bit chips of size 32MB each. Figure 3 shows the fabricated board.

Analog input board

30 channel AI card is designed to accept 30 differential high level signals having one of the following user selectable ranges.



Figure 9: 3 Channel synchro to digital converter board

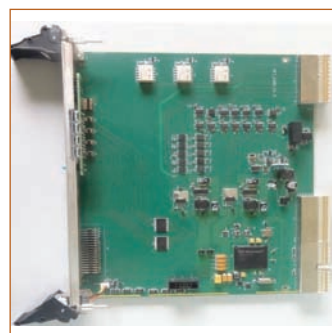


Figure 10: 3 Channel optical encoder interface board

+/-10V, +/-5V, 0-5V, -5-0 V, 0-10V. The fabricated board is shown in Figure.4.

Analog output board

4 channel analog output board is designed to generate output current of 0-20mA/4-20mA (configurable) with Channel to Channel isolation and accuracy of +/- 0.1% of FSR. The fabricated board is shown in Figure 5.

Digital input board

32 channel optically isolated digital input board has been designed with contact debouncing (configurable), 24V interrogation voltage, interrupt on status change, diagnostic features like forcing "one" and forcing "zero" are provided on the board as shown in Figure 6.

Digital output board

32 channel optically isolated digital output board has been designed with current sink capacity of 10mA per channel and output voltage limited to 30V. Diagnostic features like read-back from optocoupler output signal and watchdog timer for generating failsafe output are provided on board. The fabricated board is shown in Figure 7.

Relay output board

16 channel relay output board is designed with 24Vdc coil operating voltage and 28Vdc/2A contact rating. Normally open or closed contact configurations are jumper selectable. Watchdog timer with programmable timeout period is provided to ensure that relays go to de-energized state in the absence of tick pulse from the CPU. Relay contact read-back facility is provided to ensure proper output to the final control element in the plant. The fabricated board is shown in Figure 8.

Synchro to digital converter board

3 Channel Synchro format inputs (Reference 1-130Vrms) using Continuous Conversion, Tracking Converter (20RPS) with resolution 12 bits and accuracy of ± 1.3 arc minutes. As part of diagnostics, Inhibit input, Converter busy outputs are available. The fabricated board is shown in Figure 9.



Figure 13: 8 Channel thermocouple input board



Figure 14: cPCI RTC System Test Set-up



Figure 15: Driver installation log

Optical Encoder Interface Board

3 channel encoder interface board supports absolute Single turn or Multi-turn encoder with resolution upto 16 bits(configurable). Programmable SSI frequency range of 100 KHz (fixed) and data read back format of Gray or Binary are supported. Diagnostics features like synchronous clock read back and on board power monitoring are also provided apart from LED indication on fascia panel. The fabricated board is shown in Figure 10.

Counter timer board

This board provides 4 channel event counting up to 4G events, 12 channel frequency measurements with range 0.01Hz – 1MHz and 4 channel pulse width measurement between 250ns to 268 sec. The fabricated board is shown in Figure 11.

Leak detector board

16 channel leak detector board provides information about sodium leak status using SPLD and WTLD leak detector. The fabricated board is shown in Figure 12.

Thermocouple input board

8 channel thermocouple input board has been designed to receive k-type thermocouple signals from plant. This board provides open thermocouple detection, cold junction compensation and field isolation for k-type thermocouple. The fabricated board is shown in Figure 13.

Testing of cPCI RTC system

Linux kernel mode drivers were written for the above mentioned boards and an API library was created to access the driver functions. A test application was written using the library APIs. All boards were tested in a cPCI backplane with CPU card in system slot (slot 0) and RO/AI/DI card in one of the peripheral slots (slots 1 to 7). Figure 14 shows the test setup. Driver module and test application were put in the file system image of the CPU card. After successful booting of the kernel the driver module was installed in to the kernel using the 'insmod' command. Figure 15 shows the screenshot driver installation logs. After the driver installation, test application was run and all the features of the board were tested successfully.

Environmental and Pre-EMI/EMC qualification

Environmental and pre-EM/EMC testing were carried at facilities available in EIG for the reference system. Figure 16 shows the Environmental Chamber, Figure 17 shows Environmental test set-up and Figure 18 shows the pre-EMI/EMC test setup.

A diversified RTC system based on compact PCI bus was developed and tested to mitigate the common cause failure between two identical RTC system in existing Safety Class-2 system architecture.

*M. Sakthivel and colleagues
Electronics & Instrumentation Group*



Figure 16: Environmental test chamber



Figure 17: Environmental test set-up



Figure 18: Pre-EMI/EMC test setup

Fabrication of SiO₂ Microcantilevers using Direct Laser Writer and Wet Chemical Etching Methods

Microcantilevers (MCs) are typically rectangular-shaped beams which are fixed at one end and free at the other end with typical dimensions of 100 μm length, 20 μm width and 1 μm thickness. MCs are extensively studied for physical, chemical and biological sensing applications owing to their unprecedented sensitivity compared to conventional sensors. These devices are usually operated either in static or dynamic modes. In static mode, one side (e.g. top surface) of the MC is functionalized with a sensitive layer. When target molecules from the environment interact with the sensitized surface of the MC, differential surface stress is generated, resulting in a measurable mechanical deflection of the cantilever beam. In dynamic mode, the functionalized MCs are excited at their resonance frequency using a piezoelectric actuator. When target molecules get adsorbed on MC surface, its resonance frequency shifts to a lower value and is a potential candidate for ultrasensitive mass sensing. The bending and resonance frequency vibrations of MCs can be measured with high precision using techniques such as optical beam deflection, piezoelectric, piezoresistive and capacitance measurement methods.

MCs are conventionally fabricated from single crystal silicon (c-Si) using bulk or surface micromachining techniques. However, in recent times, MCs made of silicon dioxide (SiO₂) are gaining importance because of their larger sensitivity i.e. bending amplitude under the same experimental conditions, compared to conventional c-Si MCs. SiO₂ MCs are normally fabricated using SiO₂/Si wafer in two steps. In the first step, a desired MC pattern is transferred on SiO₂ layer by conventional UV lithography technique, while the second step involves the release of MCs from bulk silicon by either wet chemical or dry reactive ion etching of c-Si.

Although conventional lithography is straightforward in terms of execution, it has certain disadvantages. It requires pre-fabricated chrome plate masks to transfer the micropatterns, which cannot be modified and is expensive. In contrast to this, Direct Laser Writer

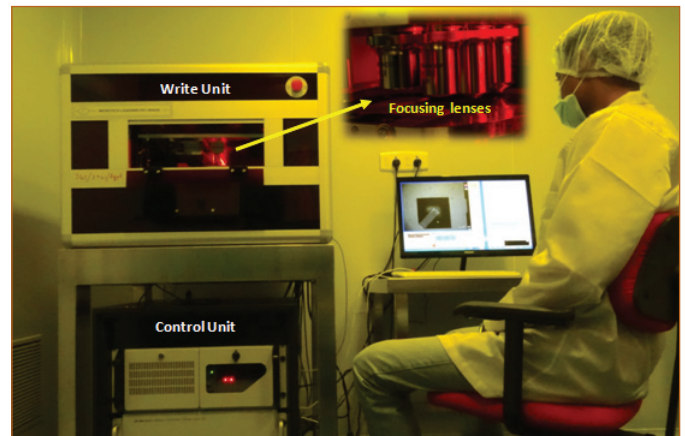


Figure 1. Direct laser writer installed inside a class-1000 clean room. Inset shows four lenses inside the write unit, with different numerical apertures to focus the laser beam (405 nm) on to the photoresist coated wafers. By optimizing various process parameters, features with ~ 1 μm resolution can be achieved using this equipment

(DLW) is a mask-less technique which offers great advantage as a rapid prototyping tool since the desired patterns can be designed and modified without the need for making new masks. In the present work, SiO₂ MCs of various dimensions are successfully fabricated using DLW and anisotropic wet chemical etching methods. Released MCs are characterized for initial bending and resonance frequency using 3D optical microscope and nano vibration analyzer, respectively.

Direct laser writer

Direct laser writer transfers the micro patterns from a preloaded soft mask on to photoresist (PR) coated wafers, using a laser beam, in serial fashion. DLW used in the present work, is installed in a class 1000 clean room (see Figure 1). It consists of two units: write unit with a 405 nm GaN laser source and a control unit with the necessary interface/software for guiding the laser beam. The parallel light rays from the laser source are acousto-optically modulated and converged through one of the available

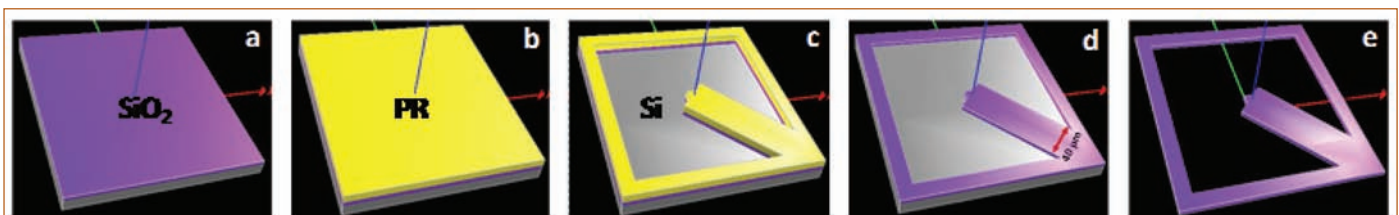


Figure 2: Various process steps involved in the fabrication of SiO₂ microcantilevers, (a) starting material: Si<100> wafer with 1 μm thick SiO₂, (b) 1 μm thick photoresist (PR) is coated using spin coater, (c) MC pattern is transferred on PR using DLW followed by buffered oxide etching of SiO₂, (d) PR is stripped using acetone and cleaned with IPA and (e) Underlying Si is etched in TMAHw solution to finally release the SiO₂ MC

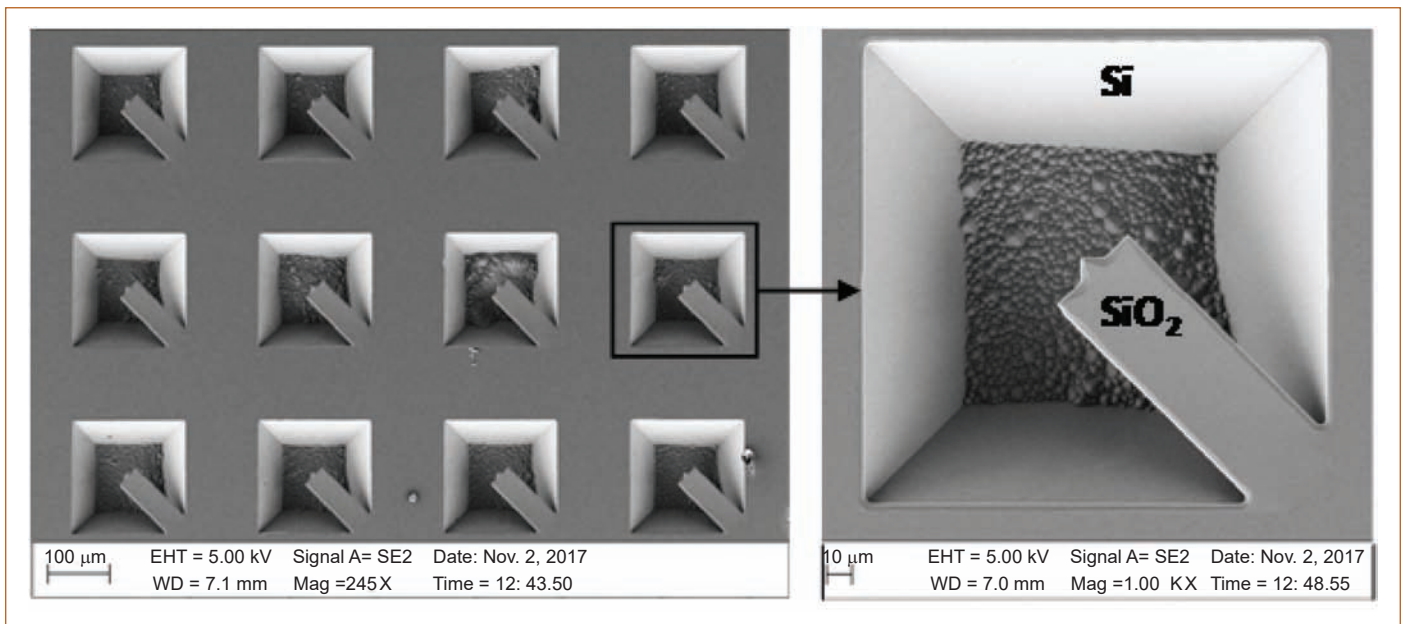


Figure 3: SEM images of the typical SiO_2 MCs fabricated in the present work. A tip at the free end is added to avoid the stiction while releasing the MCs by wet chemical etching method

four convex lenses (see inset of Figure 1). These lenses have varying magnification to control the laser beam diameter which is incident on the sample stage. The Photoresist (PR) coated wafers are placed on the sample stage and are held with a vacuum chuck. The motion of the sample stage in XY direction is controlled by interferometers with a resolution of 10 nm and the entire writing process is precisely controlled by a software. By optimizing various process parameters like laser dose, focus, diameter and writing speed, a line width of $\sim 1 \mu\text{m}$, can be easily achieved using this equipment.

Microcantilever fabrication

SiO_2 MCs of various dimensions (Length: $70\text{--}370 \mu\text{m}$, Width: $30\text{--}70 \mu\text{m}$ and T: $1 \mu\text{m}$) which are oriented in $\langle 100 \rangle$ direction of Si $\langle 100 \rangle$ wafer (45° to primary flat), were fabricated using DLW and wet chemical etching methods. It may be noted, MCs oriented in Si $\langle 100 \rangle$ direction, are relatively easy to fabricate and more stable compared to the ones oriented in Si $\langle 110 \rangle$ direction.

Various steps involved in the fabrication of SiO_2 MCs are shown in Figure 2. Si $\langle 100 \rangle$ wafer with $1 \mu\text{m}$ thick thermal oxide was used as starting material. Fabrication process started with piranha (H_2SO_4 : H_2O_2 in 3:1 ratio) cleaning of SiO_2 /Si $\langle 100 \rangle$ wafer pieces followed by spin coating of $1 \mu\text{m}$ thick positive photoresist (PR). After PR coating, wafer was pre-baked at 100°C for 60 seconds to evaporate the solvents from PR. A mask file consisting of individual MCs were created using CleWin software and loaded into DLW. The patterns were written on the PR coated wafer, using 405 nm

laser with a dose of $270 \text{ mJ}/\text{cm}^2$, such that MCs are aligned along $\langle 100 \rangle$ direction of c-Si. Post-written patterns were developed in PR developer and once the patterns are satisfactory, wafer was hard baked at 150°C for 15 min. The wafer was then etched using Buffered Oxide Etchant (BOE) for ~ 10 min in order to transfer the pattern from PR to SiO_2 layer. After oxide etching, the residual PR was stripped in acetone and cleaned with isopropyl alcohol (IPA).

Bulk Si below the patterned SiO_2 was etched using tetramethyl ammonium hydroxide (TMAH) solution, to release the SiO_2 MCs. 25% TMAH solution was diluted to 5% solution using DI water and was taken in a chemically inert alumina crucible. The solution was heated to 75°C and the wafer containing patterns were slowly immersed for etching. During the process, solution was continuously stirred with a magnetic bead. After the etching process, the wafers were removed from the solution and thoroughly rinsed with DI water, allowed to dry in ambient air and were taken for characterization. SEM image of the typical array of released MCs (Length: $110 \mu\text{m}$, Width: $40 \mu\text{m}$, Thickness: $1 \mu\text{m}$) is shown in Figure 3. It may be noted, a sharp tip at the free end of the MCs is introduced to avoid the stiction of these free standing structures to the bottom substrate while final rinsing.

Microcantilever characterization

Three dimensional (3D) profile of the released structures was measured using a non contact optical profiler that utilises white light interferometry for high resolution 3D surface measurements. All the experiments were performed in vertical scanning interferometric mode using 10X objective at room temperature. Figure 4a shows

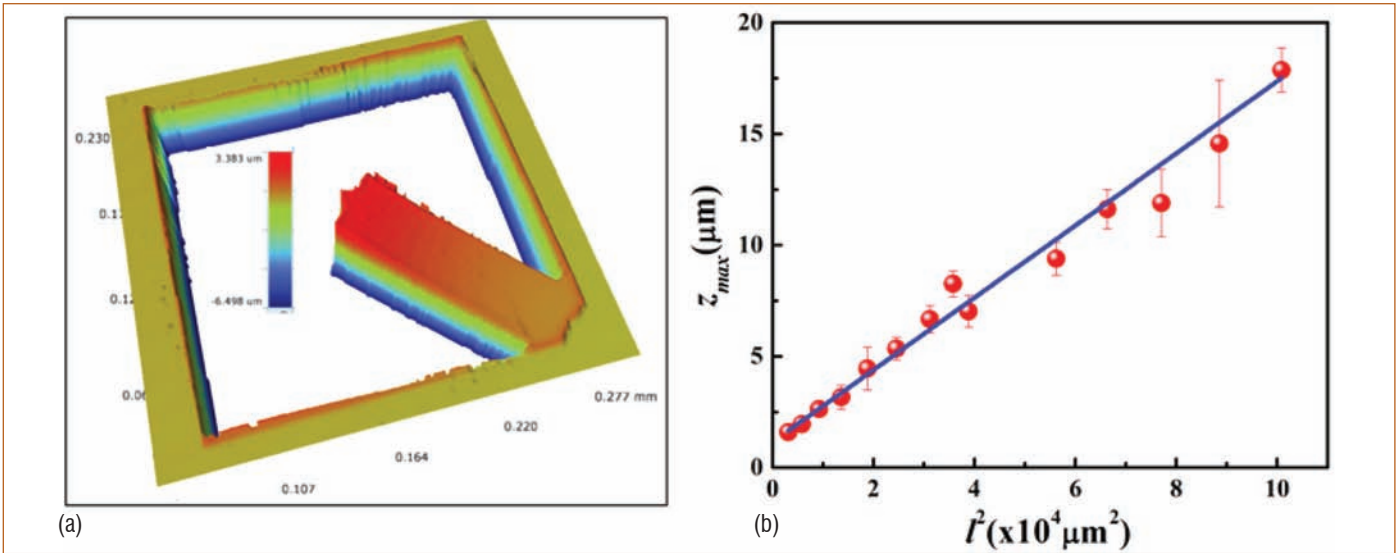


Figure 4: (a) Typical 3D profile of the released SiO₂ MC. Inherent out of plane deflection indicates the presence of gradient residual stress in the SiO₂ film. (b) Peak deflection Vs square of length of the MCs fabricated in the present work. From the slope of the linear fit of this data, gradient stress in the SiO₂ film was estimated to be 11.4 MPa

a typical 3D profile of a 110 μm long SiO₂ MC. From this figure, it is clear that the released MC is bending upwards, i.e. away from the wafer by ~ 3.4 μm. The out of plane deflection of the MC is attributed to the presence of gradient residual stress, inherently introduced during the SiO₂ film growth by thermal oxidation of c-Si. In order to estimate the residual stress, similar measurements were repeated for all the MCs with increasing length and peak deflection magnitude (z_{max}) in each case was extracted. The residual stress was estimated from a linear plot of z_{max} vs the square of the length of MCs (l^2), as shown in Figure 4b. From the slope of linear fit, the peak gradient stress (σ_{max}) was estimated using the relation, $\sigma_{\text{max}} = Etz_{\text{max}}/l^2$, where E, t and l are Young’s modulus, thickness and length of the MC, respectively. By substituting, E=73 GPa, t = 1 μm, $z_{\text{max}}/l^2 = 160 \text{ m}^{-1}$, σ_{max} in SiO₂ film used in the present work was estimated to be 11.4 MPa.

Resonance frequency and quality factor of released MCs were

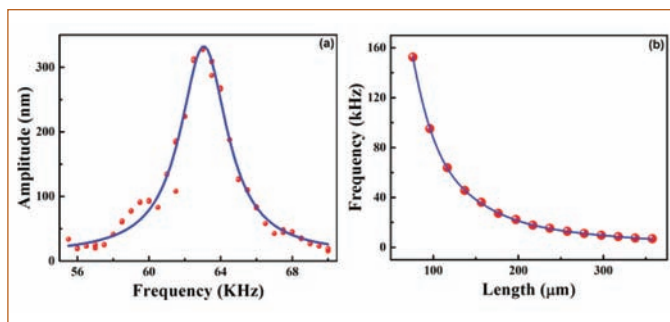


Figure 5: (a) Resonance spectrum of a typical 110 x 40 x 1 μm³ MC measured using nano vibration analyzer. From the Lorentzian fit of this spectrum, resonance frequency and quality factor were estimated to be 63 KHz and 20. (b) Variation of resonance frequency of MCs with length

measured using Nano Vibration Analyzer (NVA). NVA is a compact fiber coupled laser ($\lambda = 632.8 \text{ nm}$)-interferometric vibrometer, integrated with a precision microscope and works in non-contact mode. It can precisely measure the vibration displacement or changes in length with a high accuracy of ~ 0.1 nm over a wide range of frequencies upto 10 MHz. To measure the resonance frequencies of the MCs, the wafer containing MCs was glued on a piezo actuator which in turn was excited using a function generator. By varying the function generator frequency in required steps amplitude of vibration was recorded using NVA at each frequency. The resonance frequency of the MC was estimated from the plot of frequency versus amplitude. Figure 5a shows a typical resonance spectrum of 110 μm MC along with lorentzian fit, from which resonance frequency and quality factor values were estimated to be 63 KHz and 20, respectively. Similar measurements were repeated for all the MCs and the resonance frequency Vs length of the MCs is shown in Figure 5b. From this figure, it is clear that resonance frequency of the MCs decrease with increasing length and has an inverse square dependance.

To conclude, SiO₂ MCs of various dimensions are successfully fabricated using DLW and wet etching of Si by TMAH. Both bending (deflection) and resonance frequency measurements confirm that SiO₂ MCs are indeed released and indicate the presence of inherent residual stress. Studies are underway to explore these MCs for various sensing applications like humidity, temperature and gamma radiation.

*K. Prabakar and colleagues,
Materials Science Group*

Young Officer's FORUM

High Temperature and Vacuum Tribological Properties of Ultrananocrystalline Diamond Thin Films

Tribology is derived from the Greek word *tribos*, which means "rubbing" and it is defined as the study of two surfaces in relative motion under the application of load, leading to friction and wear. The coefficient of friction is defined as the ratio of frictional force to normal load. Fundamentally, it is proportional to the normal load and depends on the real area of contact. Low friction and high wear resistance properties of materials are desirable for efficient and durable sliding devices. The carbon based materials are attractive for tribological purposes due to tunable hybridization state of carbon atom. The deposition of crystalline diamond films onto the relevant bulk materials are widely used for several applications such as cutting tools, mechanical assembly components and bio-devices due to their unique microstructure and chemical properties. Diamond is a wide band gap material with high thermal conductivity, extreme hardness, high elastic modulus, low friction and high wear resistance properties. All these outstanding properties of diamond are associated to the sp^3 -hybridized chemical bonding state of carbon atoms in cubic tetrahedral unit-cell parameter. Depending upon the grain size, the diamond films can be further categorized into micro, nano and ultrananocrystalline diamond films.

The tribological properties of ultrananocrystalline diamond (UNCD) films are found to be superior compared to their micro/nanocrystalline counterpart. This improvement is associated to unique morphology and microstructure of ultranano diamond grains surrounded by amorphous carbon (a-C) and graphitic phases occupying the wider grain boundaries. Notably, the improved tribological properties of crystalline diamond including UNCD films are generally explained by the existing tribo-mechanisms i.e. passivation and graphitization of the sliding surfaces. In the passivation mechanism, the film surface being chemically inert is not much deformed and which provides mechanical stability to the sliding surfaces. In contrast,



Ms Revati Rani is working as Scientific Officer in Materials Science Group. She is from 8th batch of BARC Training school at IGCAR campus. She has completed her M.Sc. (Physics) from Kurukshetra University, Haryana in 2012. She is currently pursuing her Ph.D (Physical Sciences) from HBNI under the guidance of Dr. Niranjana Kumar. Her research interest includes tribo-chemical investigation of low friction mechanisms in nanocrystalline diamond films under high-temperature and high-vacuum conditions.

the transformation of sp^3 crystalline diamond into sp^2 and α -C phases is responsible for the deformation of the sliding surfaces. The tribo-test environment including the internal chemical structure of films are governing factors for determining passivation and/or graphitization mechanisms. The tribological properties of UNCD thin films are investigated in (a) ambient atmosphere and room temperature (AART) (b) high vacuum $\sim 5 \times 10^{-6}$ mbar and room temperature (HVRT) and (c) high-temperature ~ 623 K and high-vacuum $\sim 5 \times 10^{-6}$ mbar (HTHV) tribo-environmental conditions. Raman spectroscopy and X-ray photoelectron spectroscopy (XPS) were used to explore the chemical nature of sliding surfaces which further helped to understand the underlying tribological mechanisms.

UNCD film morphology shows homogeneously distributed nanowire like feature with length of 200-300 nm (Figure 1a). Each nanowire consists of diamond grains of size ~ 5 nm as core embedded with sp^2 -bonded carbon (nanographite or amorphous carbon) as shell. It is clearly shown in the high-resolution transmission electron microscopy (HRTEM) image (Figure 1b). The FT_1 and FT_2 Fourier-transformed diffractograms confirm that the core and shell consists of diamond and sp^2 -bonded carbon, respectively. The bonding structure of UNCD films are comprehensively investigated by Raman spectroscopy and XPS (Figures 1c to 1f). In Raman spectra, the ν_1 (1168 cm^{-1}) and ν_3 (1510 cm^{-1}) bands correspond to transpolyacetylene (TPA) phases and D (1329 cm^{-1}) and G (1582 cm^{-1}) bands are signatures of a-C and graphitic phases, respectively (Figures 1c and 1d). These Raman bands are fingerprint of ultrananocrystalline diamond films. The $I(D)/I(G)$ ratio of UNCD film at room temperature (RT) is 1.65 which decreased to 1.52 while exposed to temperature of ~ 623 K. This temperature parameter

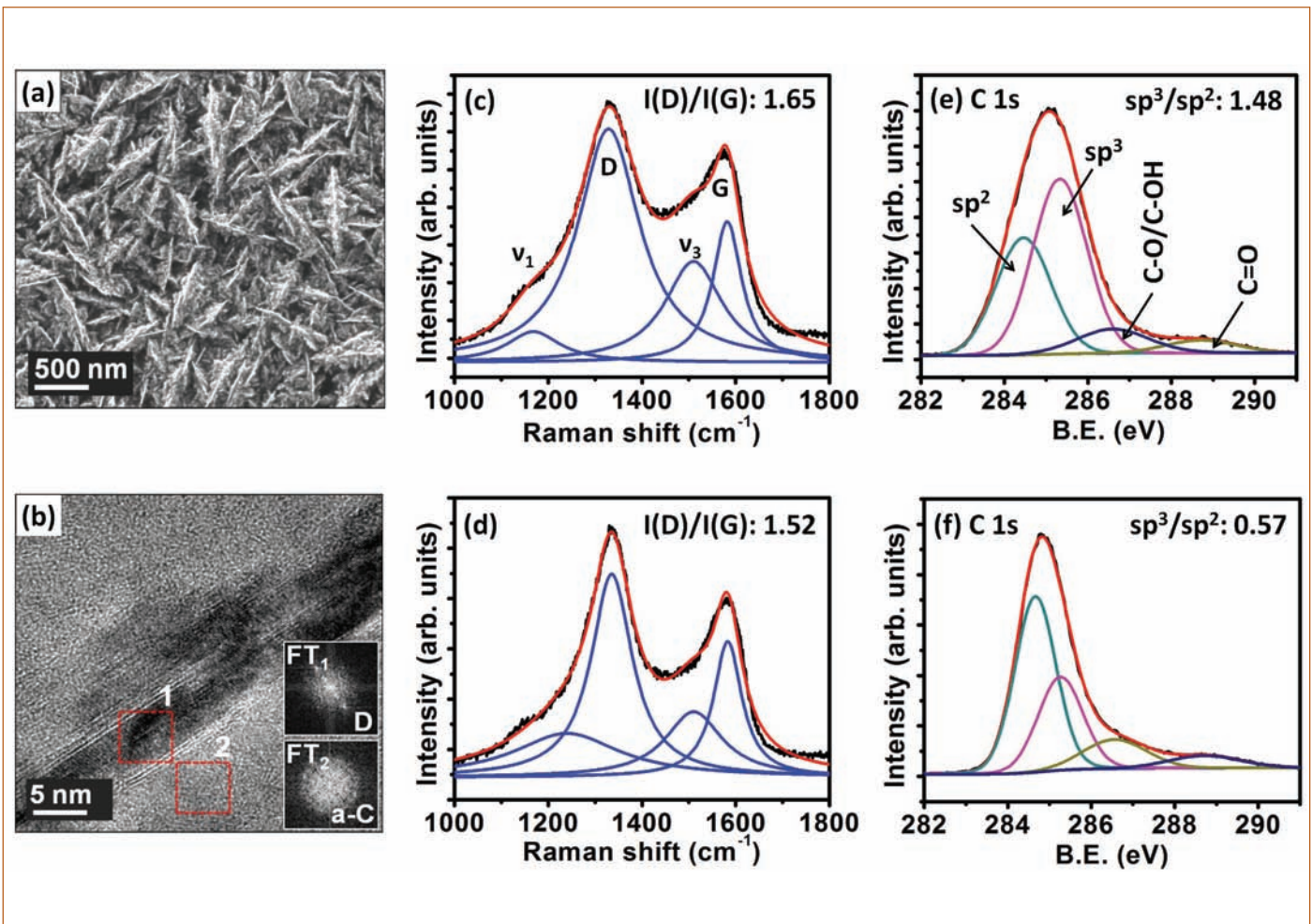


Figure 1: (a) SEM image of UNCD film surface and (b) HRTEM image of typical nanowire feature of UNCD film surface. The insets FT₁ and FT₂ show the Fourier-transformed (FT) diffractogram images corresponding to regions 1 and 2, respectively. (c and d) Raman spectra and (e and f) XPS: (c and e) UNCD films surface and (d and f) UNCD film surface at RT exposed to temperature of ~ 623 K

is used for high temperature tribology measurements of UNCD films and it will be discussed below. A broad C1s photoelectron emission spectrum is deconvoluted into four peaks at the binding energies of 284.46, 285.3, 286.6 and 288.7 eV (Figures 1e and 1f). The first two peaks are designated as sp² and sp³ hybridized carbon and third and fourth one correspond to oxygen functional groups i.e. carboxylic (C-O/C-OH) and carbonyl (C=O) groups, respectively. The sp³/sp² ratio for UNCD film surface is 1.48 at RT and decreased to 0.57 while exposed to temperature of ~ 623 K.

Friction and wear behavior of UNCD films distinctly differ depending upon the tribo-test environment (Figure 2). Normal load 0.5 N, linear sliding speed 0.5 cm/sec and alumina (Al₂O₃) ball of 6 mm diameter are used for friction measurements. The tribo-tests are conducted in three different tribo-conditions of AART, HVRT and HTHV. The saturated value of friction coefficient is ~ 0.023 in AART (Figure 2a) which significantly increased to ~ 0.17 in HVRT (Figure 2b) and in addition, early film failure was noticed. However,

the friction value decreased to superlow value of ~ 0.002 in HTHV (Figure 2c). Raw friction data are presented as black curves in all three cases. Wear dimension is found to be directly proportional to friction value and it is lowest in HTHV compared to other two tribo-conditions (Figure 2d).

The deconvoluted Raman spectra of wear tracks and ball scars are shown in Figure 3 for all three tribo-conditions. For comparison purpose, all parameters of the Raman spectrometer were kept same. Chemical structure and I(D)/I(G) ratio of the wear track is quite similar to the UNCD film surface in AART (Figure 3a). Chemical stability of the UNCD structure can be explained by passivation mechanism of sliding surfaces by ambient atmospheric chemical species. Similar Raman shift at the ball scar clearly indicate carbonaceous transfer film formation (Figure 3b). Moreover, a decrease in I(D)/I(G) ratio and blue shift in D and G bands are observed at the ball scar area compared to the wear track. These observations point toward the shear induced a-C to graphitization

in AART. The Raman peak parameters such as peak shape, peak position, I(D)/I(G) ratio and TPA phase of UNCD structure in wear track in HVRT are also quite similar to the wear track formed in AART (Figure 3c). However, the chemical structure of carbonaceous transfer film formed at the ball scar is completely transformed into a-C and t-aC structure. This is noticed by the significant change in peak shape, peak position and modified I(D)/I(G) ratio as shown in Figure 3d. In this condition, the blue shift in D and red shift in G bands is observed compared to the carbon structure of the corresponding wear track. Here, TPA phase is completely disappeared which could be a strong indication for the conversion of UNCD into a-C and t-aC structure. This could be possible due to high frictional energy which provides activation energy for such conversion. Therefore, in HVRT, the ball scar is fully covered with transfer film of a-C and t-aC phases. Thus, in this particular

condition, sliding occurred between UNCD film and a-C/t-aC structure formed on the ball side. Distinct changes in Raman spectra of the sliding surfaces in HTHV are observed (Figure 3e & 3f). The I(D)/I(G) ratio of UNCD film exposed to temperature of ~623 K is 1.52 which is slightly less than the UNCD film at RT as shown earlier (Figure 1c & 1d). Moreover, at HTHV, the D and G bands are blue shifted, indicating temperature induced annealing which tends to reorient the carbon structure into more ordered sp² phase. The I(D)/I(G) ratio significantly decreased to 0.96 in the wear track compared to the film surface (Figure 3e) and it is contrasting to the wear track formed in AART and HVRT as mentioned above. This indicates that the contact pressure at high-temperature in high-vacuum tribo-condition is a deterministic factor to reorient a-C into ordered sp² phase. Moreover, sp³ to sp² phase conversion is also possible depending upon the activation energy

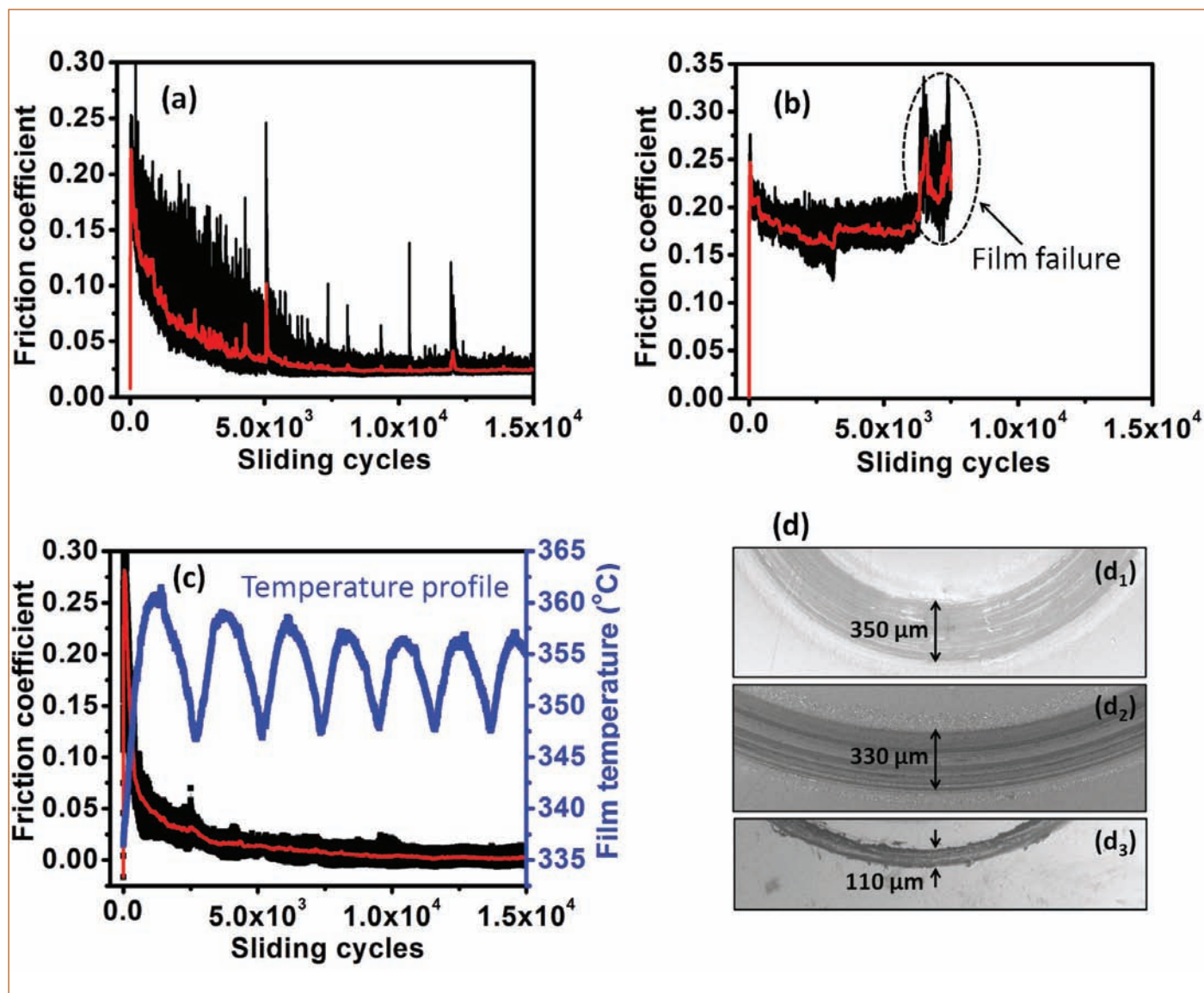


Figure 2. Friction coefficient vs sliding cycles of UNCD films: (a) AART, (b) HVRT, (c) HTHV, black curves are raw friction data and red lines are fitted curves and (d) FESEM images of the corresponding wear tracks for (d₁) AART (d₂) HVRT and (d₃) HTHV

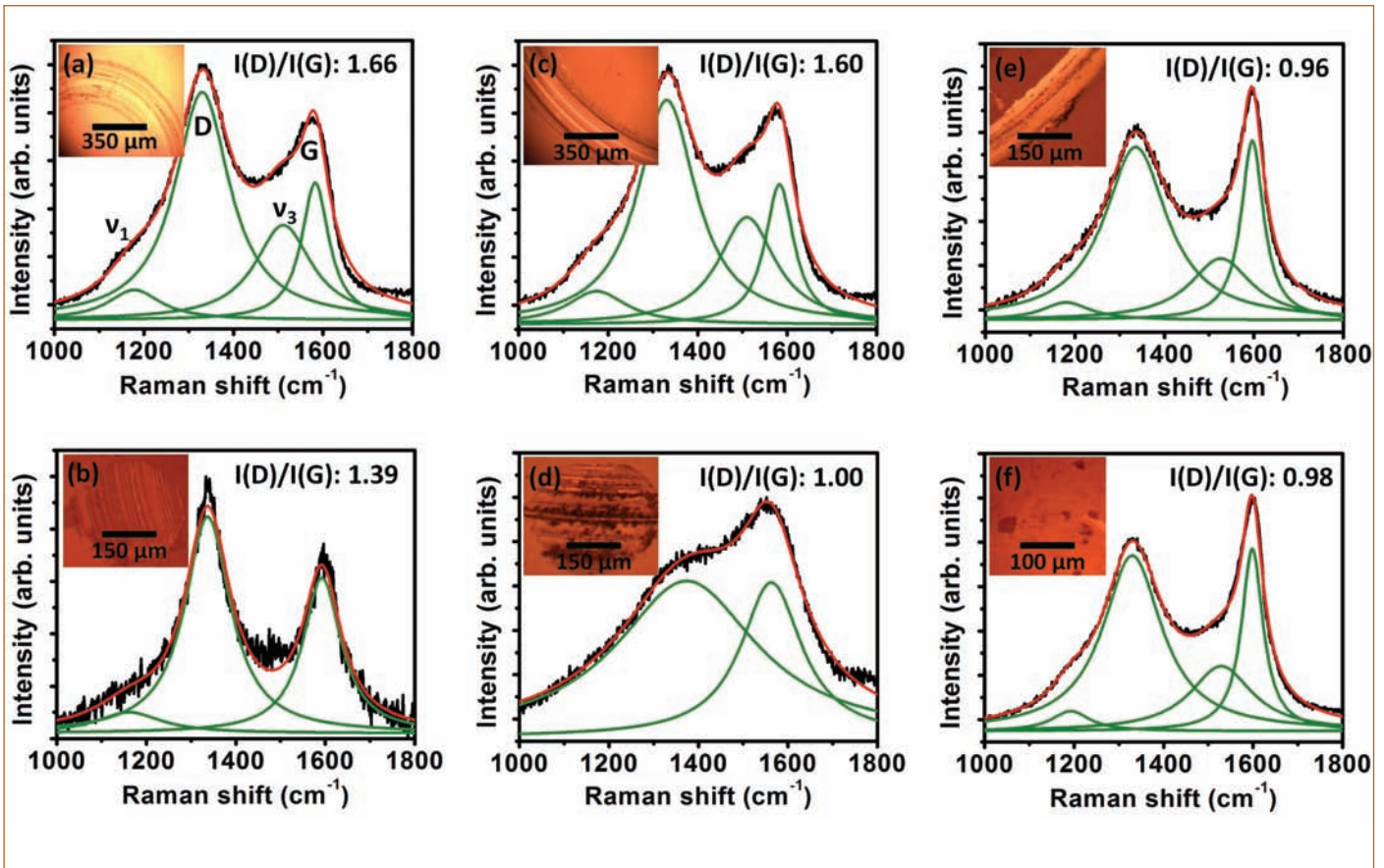


Figure 3: Raman spectra: (a and b) AART (c and d) HVRT (e and f) HTHV; (a, c and e) inside the wear track of UNCD films and (b, d and f) corresponding alumina ball scars; Optical images of wear tracks and corresponding alumina ball scars are also embedded for each tribo-condition

which can be provided by both temperature and contact pressure. It is worth mentioning that the Raman spectroscopy is a bulk sensitive technique and therefore, formation of above mentioned carbon phases is a bulk phenomenon.

The XPS study is carried out for more insightful surface chemical analysis of transfer film deposited on the ball contact area during the sliding process. The spatial resolution of XPS was $50\ \mu\text{m}$ and therefore, it was possible to focus the X-ray at specific locations inside the wear scar regions on the ball contact surface. Survey XPS shows well resolved C1s and O1s photoelectron shifts on the ball scar region in all three different tribo-conditions which is signature of the carbonaceous transfer film formation with adsorbed oxygen content (Figure 4). In survey spectra, the C/O ratio is less 0.51 in AART and intensity of the alumina peaks Al2p and Al2s is strong (Figure 4a). HR-XPS of C1s photoelectron shift shows well-resolved deconvoluted sp^2 and sp^3 peaks with the contribution of oxygen functional groups (Figure 4b). The sp^3/sp^2 carbon ratio is 0.65 which is much lower compared to virgin film surface (1.48) and it is an indicative of tribo-chemical conversion of sp^3 to sp^2 phase (Figure 1e). In survey spectra, C/O

ratio is 0.68 on ball scar in HVRT (Figure 4c). In this condition, contribution of oxygen contamination is mainly due to exposure of film sample in ambient atmosphere after conducting the tribo-tests. Moreover, HR-XPS shows significant increase in sp^3/sp^2 ratio to 1.88 (Figure 4d). These values are much higher compared to AART. Furthermore, the sp^3/sp^2 ratio is even higher than the virgin film surface. This is possibly associated to the conversion of sp^2 into amorphous carbon (a-C) and disordered sp^3 (t-aC) phase in HVRT. This evidence is supported by Raman spectroscopy (Figure 3d). The above mentioned phase transformation is possible due to high activation energy which is provided by high frictional energy in HVRT. In survey spectra, C/O ratio is much higher 2.46 on ball scar in HTHV compared to other tribo-conditions (Figure 4e). Interestingly, sp^3/sp^2 ratio of transfer film is reduced to 0.46 on ball scar in this tribo-condition (Figure 4f). These values are lower than the film surface exposed to temperature of $\sim 623\ \text{K}$ (0.57) (Figure 1f). This directly indicates the significant conversion of sp^3 into sp^2 phase. Such conversion is also evident in AART to some extent but high temperature is energetically favorable for such transformation. Stress-induced conversion of sp^3 into sp^2 phase is dominating in AART while both stress and thermal energy are governing factors for

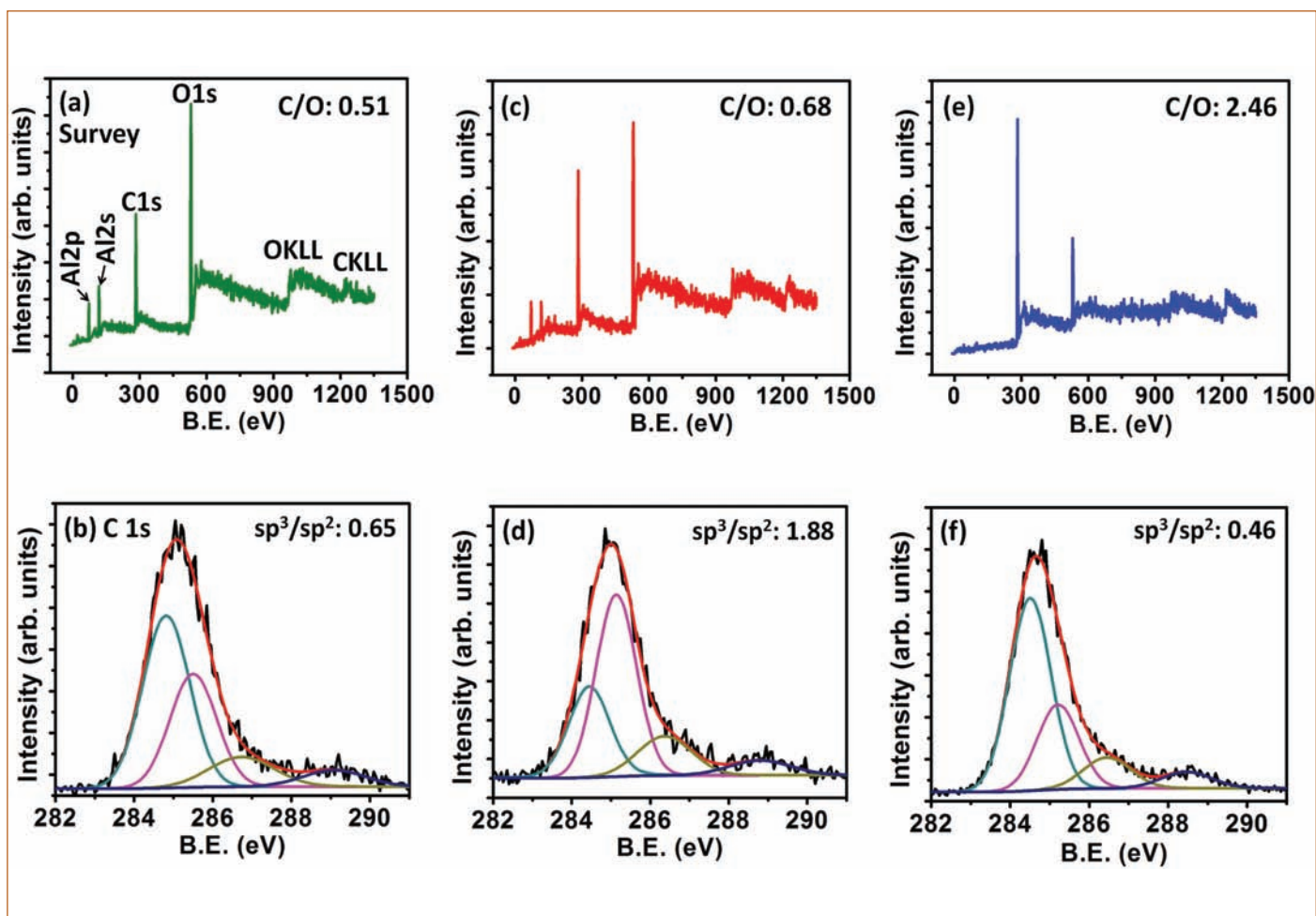


Figure 4: XPS spectra: (a and b) AART (c and d) HVRT and (e and f) HTHV; (a, c and e) Survey XPS and (b,d and f) corresponding C1s HR-XPS of alumina ball scars

such conversion in HTHV. Chemical characteristics of transfer film in AART and HTHV are contrasting to HVRT. The amorphization is dominated in HVRT while graphitization occurs in AART and HTHV. The tribo-induced conversion of ordered sp^2 and sp^3 phases after the amorphization state is restricted in HVRT. However, nucleation of ordered carbon phase in AART and HTHV is realistic due to favorable activation energy.

In summary, the tribological properties of UNCD films were investigated in AART, HVRT and HTHV. HRTEM analysis directly showed ultranano diamond grains in UNCD film which was further supported by Raman spectroscopy. Moreover, phase composition of UNCD films was investigated by XPS analysis which showed significant amount of sp^3 phase of ultranano diamond grains and a-C/ sp^2 phases occupying the grain boundary. Raman

spectroscopy and XPS confirmed the tribo-environment dependent changes in UNCD structure in wear track and ball contact area. Friction coefficient was significantly high ~ 0.17 in HVRT. In this case, passivation mechanism was restricted and frictional shear transformed the diamond sp^3 into a-C and t-aC phases. However, passivation and graphitization were energetically favorable mechanisms in AART which reduced the friction coefficient to ~ 0.023 . Moreover, significant conversion of diamond sp^3 into hydrogenated graphitized phase was predominant mechanism for the superlow friction coefficient ~ 0.002 and ultrahigh wear resistance in HTHV.

Revati Rani
Materials Science Group

Young Researcher's FORUM

Alloy 617: The Avenue of Tomorrow's Advanced Ultra Supercritical Thermal Power Plant

India along with the world is facing tough challenges of the global warming and usage of fossil fuels at a lower efficiency raises concern among philanthropist research community. Tackling both these issues in one go requires raising the boiler operating temperature over 1023 K and pressure up to 25 MPa. However, toward achieving this goal, a judicious selection of proper materials for the ducting, heat exchanger and transition liner in gas turbines ensuring resistance to creep deformation, corrosion resistance, and long-term microstructural stability are major technological challenges for researchers. In this endeavor, where the conventional high-temperature materials like ferritic–martensitic steels (P91, P92) fall short of these requirements, the use of Ni-based superalloys is showing a promising potential owing to their better creep rupture life and corrosion resistance in the operating conditions.

Alloy 617 is a class of Ni-based superalloys having a face-centered cubic (FCC) structure developed solely to serve as a backbone for the advanced ultra-supercritical (AUSC) coal-fired thermal power plants in India and around the globe. The genetic make-up of this alloy is so chosen to operate this material successfully in the temperature and pressure conditions well over 1023 K and 25 MPa respectively. The major alloying elements present in the Alloy 617 are shown in Table 1. The high nickel and chromium content offers the alloy a very high resistance to variety of reducing and oxidizing environments. The presence of aluminum, in conjunction with the chromium, provides oxidation resistance at elevated temperatures by a phenomenon well known as selective oxidation mechanism. Solid-solution strengthening is imparted by the cobalt and molybdenum. In addition to solid solution strengthening, molybdenum also offers the stability of the oxide layer formed by chromium and aluminum.

Table 1: The major alloying elements present in Alloy 617

	Ni	Cr	Al	Co	Mo	Ti	Fe
Wt. %	Bal.	22.1	1.2	11.6	9.4	0.4	0.12
	Mn	C	Cu	Si	S	N	Nb
Wt. %	0.01	0.06	0.01	0.1	0.001	0.005	0.02



Dr. Aditya Narayan Singh obtained his Bachelor's degree in Electrical and Electronics Engineering from UPTU, Lucknow. He completed his MS in Nanoscience Nanotechnology from Gujarat Forensic Sciences University, Gandhinagar, Gujarat, and secured University Gold Medal. He joined IGCAR as a Junior Research Fellow in Materials Technology Division, Metallurgy and Materials Group in April 2014 and carried out his doctoral work under the guidance of Dr. Aniruddha Moitra from HBNI. His doctoral thesis is on "Study of Deformation and Fracture Behaviour of Alloy 617".

In the light of above advantages, it is imperative to study various mechanical and microstructural characterizations to explore more about Alloy 617 to understand structure-property relationship. To understand the performance of this material under real time plant operations, artificial aging has been done to study the performance of the material in close resemblance to real time operations.

Mapping the hierarchical microstructure during aging

To understand the aging induced microstructural evolution, Alloy 617, has been aged at 1023 K at different length scale up to 20 kh aging. The microstructural evolutions over aging are shown in Figure 1. A substantial presence of annealing twins have been noticed in the as-received microstructure as shown in Figure 1a. The presence of annealing twins is an indication towards lower stacking fault energy (SFE) of this material. These serrations in the 1 kh aged alloy (Figure 1b) indicate that there are indeed small

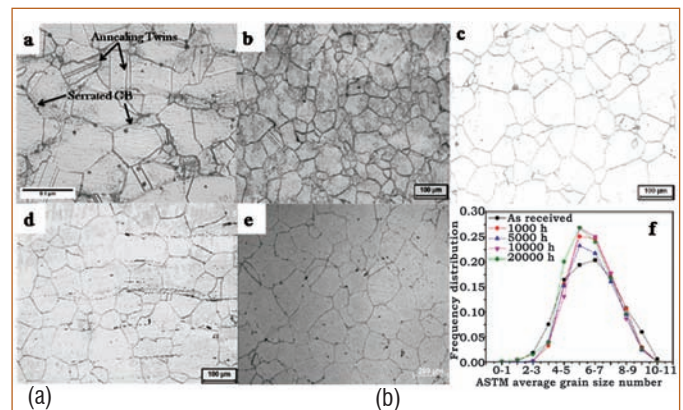


Figure 1: The mapping of hierarchical microstructure evolution during the aging: (a) as-received, (b) 1 kh, (c) 5 kh, (d) 10 kh, (e) 20 kh and (f) Frequency distribution of Grain size during aging



Figure 2: The hardness profile of Alloy 617

amounts of grain movement and coarsening does occur during high temperature exposure. One likely explanation for the serrations in the grain boundaries is that secondary phases such as carbides might have interlocked during the grain boundary migration, thus causing the irregular boundary. The carbide banding present in 1 kh aged alloy now appears seemingly difficult to identify in 5 kh aged alloy due to large numbers of $M_{23}C_6$ precipices evolution (Figure 1(c)). The extensive precipitation of carbides is one of the salient features of 10 kh aged alloy (Figure 1(d)). The extensive precipitations of carbides in 20 kh hours have now coarsened to a large extent (Figure 1(e)). Though, there have been increments in grain boundary carbides, serrations appear and disappear

over aging, and carbides coarsens but the salient features of the microstructures in Alloy 617 are grain size remaining fairly constant within the ASTM number 4-6 as observed from the frequency distribution profile in Figure 1(f).

Hardness Profile of Alloy 617

Hardness of the Alloy 617 in its as-received and aged conditions were measured at room temperature (RT) by a Vickers hardness tester with a dwell time of 15 seconds at a 40X magnification, and the results are reported in Figure 2. Though there has been usual scatter in the hardness data, a clear trend in the variation of hardness can be observed. In the as-received condition, alloy displayed its lowest hardness value of ~ 196 HV, whereas the aged alloy shows improved hardness even after aging duration of 1 kh. The hardness of this alloy increases consistently for the aging treatment up to 5 kh. This could be attributed to the simultaneous occurrence of the $M_{23}C_6$ and γ' precipitates leading to the overall strengthening of the matrix. There is a marginal drop in hardness between the aging treatment of 5 and 10 kh. For the aging treatment from 10 to 20 kh, it is tending towards a marginal increase at around 250 HV.

The unusual flow behavior of γ'

The tensile tests on the Alloy 617 for the as-received and thermally aged conditions have been carried out at the room temperature (298K) at a nominal strain rate of $3 \times 10^{-3} s^{-1}$. The engineering stress vs engineering strain plot for the as received and aged conditions are shown in Figure 3a. It is evident that the thermal

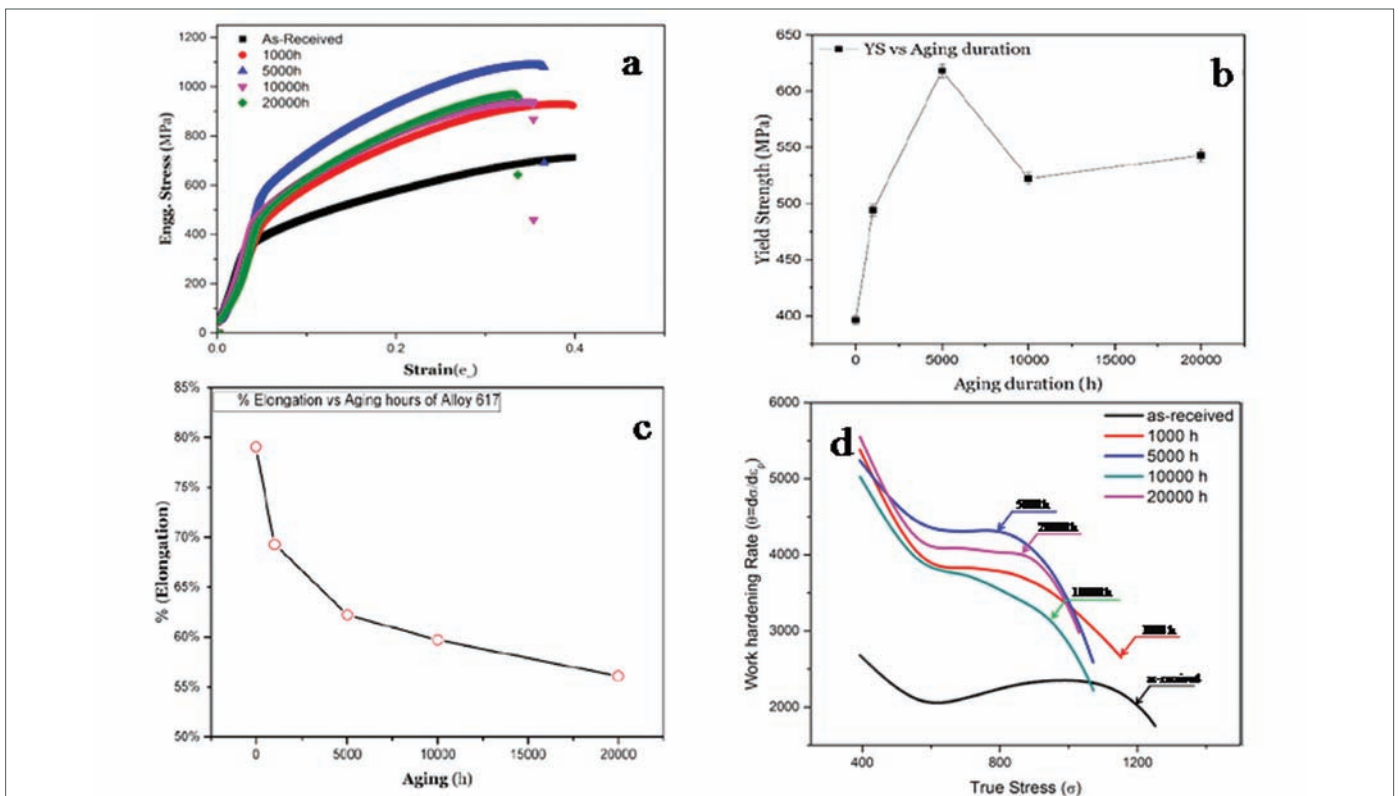


Figure 3: Profile plots of various mechanical parameters of Alloy 617 for as-received and aged material, (a) engineering stress vs strain, (b) Variations of YS, (c) Variation of % elongation and (d) Combined plot of θ vs σ for all aged samples

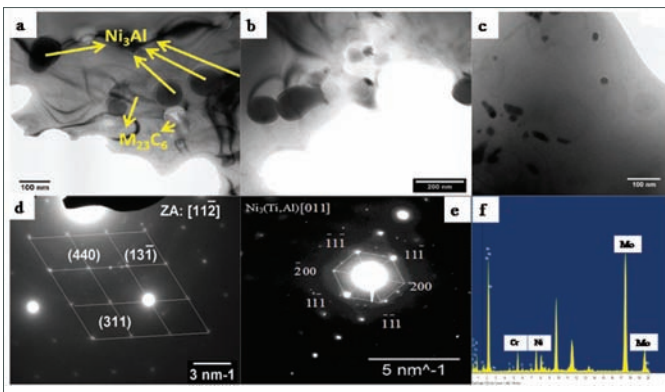


Figure 4: Bright field TEM image and SAED pattern of Alloy 617 aged at 1023: (a) Spheroidal γ' in 5 kh; (b) γ' of size 80–100 nm; (c) Unidentified precipitates; (d and e) corresponding SAED pattern to a and b and (f) EDS analysis of (c)

aging has made significant influences towards the deformation characteristics of this alloy. Variations of yield stress (YS) and % tensile elongation (TE) with aging duration of the Alloy 617 in both as-received and aged conditions are shown in Figure 3b and 3c respectively. Yield stress (YS), as shown in Figure 3b, initially increases up to 5 kh of aging, then decreases in the 5 – 10 kh aging duration and finally shows a marginal increase in the regime of 10 – 20 kh aging duration. It has been observed that unlike the yield stress variation, the tensile ductility, as measured the % total elongation (TE) consistently decreases with the aging duration, as shown in Figure 3c. To get insight into the work-hardening behavior of the Alloy 617, the instantaneous work-hardening rate $\theta = d\sigma/d\epsilon_p$ is considered as is plotted against σ as shown in Figure 3d.

This unusual behaviour of yield strength and TE invites various contributing factors for instance: type, morphology, shape and distribution of the precipitates to be looked upon to corroborate the flow of dislocation in this material. The role of stacking fault energy (SFE) to the deformation mechanism also needs to be considered while explaining this unusual behaviour. The presence of annealing twins in solution annealed condition is an indication for this material with low SFE ($\sim 30 - 40$ mJ/m²) energy. Alloy 617 being a material with low SFE is prone to planar slip in deformation, where the motion of dislocations is more strongly influenced by the nature and distribution of the precipitates, as compared to the higher SFE materials with higher tendency for cross slipping.

The representative TEM images of 5, 10 and 20 kh aged material is shown in Figure 4 to clearly demonstrate what is the basic mechanism behind this abnormal behaviour of tensile property in this material. The morphology of γ' precipitates (shown in Figure 4a and corresponding SAED pattern (d)) in 5 and 1 kh aged condition remains unaltered bearing the same spherical nature. A marginal growth in size $\sim 80 - 100$ nm has been observed with respect to 1 kh aged material. It is well appreciated that the presence of γ' precipitates in the matrix of an aged alloy of this material plays a

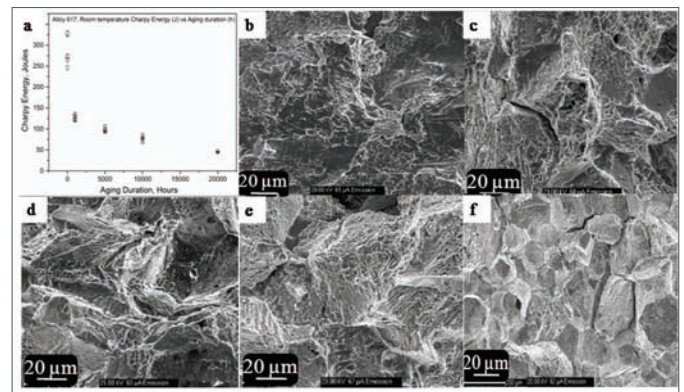


Figure 5: The Charpy energy and fractographs of Alloy 617: (a) Charpy impact energy; (b) as-received; (c) 1 kh; (d) 5 kh; (e). 10 kh and (f) 20 kh

crucial role in imparting strength at higher temperature. However, there are indications that it only grows due to thermal aging, but to a limited extent. It could be appreciated that even this marginal change in the precipitate size may have significant influence on the deformation characteristics of this material. The morphology of γ' precipitates in 10 kh is shown in Figure 4b and corresponding SAED pattern is shown in Figure 4e. The γ' precipitates have grown further along with $M_{23}C_6$ carbides (not shown here) is one of the major reason for the sudden drop in YS from 5 to 10 kh aged material. Aging further up to 20 kh has improved the YS which can be seen through a tendency of increment in YS plot of this material. The exact reason has not been identified at this stage, but it is certain that some new finer precipitates has evolved with the aging which can be seen in Figure 4c. Though, these finer precipitates also have not been identified, but their elemental analysis ascertain that these are rich in Ni, Cr and Mo. These fine precipitates have once again pushed up the YS even at 20 kh aging durations at 1023 K. This behaviour though abnormal, is a contributing factor toward high temperature application of Alloy 617. All the $\theta - \sigma$ shows clear three stage behaviour at all aging durations: (1) stage I; an initial transient stage (TS), with decreasing θ , (2) stage II; θ increases gradually and attains a local maximum, and (3) stage III; where θ gradually decreases. This alloy exhibits anomalous work-hardening characteristics for the different aged conditions. There has been a sudden rise in the work hardening from as-received to 1, 5, and then a sudden drop at 10 kh. There is again an increasing tendency in the work-hardening behavior after 20 kh of aging. This feature is attributed to the aging induced γ' evolution, a slight coarsening, and then dissolving in the matrix (evolution of γ' - coarsening–dissolve–new precipitates).

Fracture properties of the alloy 617

To evaluate the fracture properties of this material, the as-received and aged materials are subjected to Charpy impact test. The Charpy impact specimens are in compliance with the ASTM E-23-05 standards. The variation of Charpy impact energy (J) with aging

Table 2: KV, A_g , Δa_m , UTS, and crack initiation J values for Alloy 617

Material condition	KV (J)	A_g	Δa_m (mm)	UTS (MPa)	J_0 (kJ/m ²)	$J_{0.2}$ (kJ/m ²)	$J_{0.2t}$ (kJ/m ²)
As-received	285.17	0.39	0.85	1251.4	1248.86	824.33	1154.4
1000 h	127.33	0.28	0.66	1543.2	305.19	330.73	334.22
5000 h	98.16	0.26	0.63	1721.0	209.38	248.75	248.71
10000 h	77.60	0.27	0.64	1481.7	169.71	198.76	198.56
20000 h	460.00	0.24	0.58	1496.8	84.84	112.63	112.13

duration (h) is shown in Figure 5a. This material shows high impact energy (285.16 J) in the as-received condition, but a sharp reduction of ~ 80 % w. r. to as-received material has been noticed in 20 kh aged material. Fractographic investigations of as-received material reveal ductile failure which is indicated by the presence of fibrous dimples as shown in Figure 5b. The 1 kh aged alloy shows a signature of transition from predominantly ductile one to predominantly intergranular mode of fracture as in Figure 5(c). Aging for 5 kh has embrittled the grain boundary further or if not, it has started to show its presence as can be seen in fractographs of Figure 5 (d). The huge drop between the Charpy impact energy of 1 kh (~130 J) and 5 kh (~98.16) has a good conformity with the fractographs. Aging over longer duration of 10 kh and 20 kh as shown in Figure 5 (e-f) respectively, agrees with the Charpy impact energy value.

The presence of microcracks and microvoids act as initiation sites and provide an easy way for the crack to propagate during the Charpy impact test (~ 77.6 J) and ultimately lowering the fracture toughness of this material in 10 kh aged material. Though the aging durations from the 10 to 20 kh is two-fold, the fractographs have not demonstrated much variation in their morphologies and this is in tune with Charpy impact energy (~44 J) too.

$$J(\Delta a) = 11.44 * KV * (Ag)^{1/3} * \Delta a^{2/3} \quad (1)$$

Where J is J integral, KV is Charpy fracture energy, A_g is uniform fracture strain, and Δa crack extension.

The blunting line can be given as:

$$J = s_1 * \Delta a = 3.75 * R_m * \Delta a \quad (2)$$

Where J is J integral, R_m is ultimate tensile strength and, Δa crack extension.

J at crack initiation can be obtained as an engineering evaluation in three different ways. J_0 is obtained by the intersection of the linear extrapolation of the J-R curve from the range $\Delta a > \Delta a_m$ to the intersection with the blunting line. $J_{0.2}$ is the value of J at $\Delta a = 0.2$. $J_{0.2t}$ is the J value at 0.2 mm from the intersection with the blunting line. From these definitions the three quantities are obtained as follows:

$$J_0 = \frac{(7.33 * KV * A_g)}{(1 - 1.47 KV / R_m)} \quad SE \quad (3)$$

$$J_{0.2} = 3.92 * KV * (Ag)^{1/3} \quad (4)$$

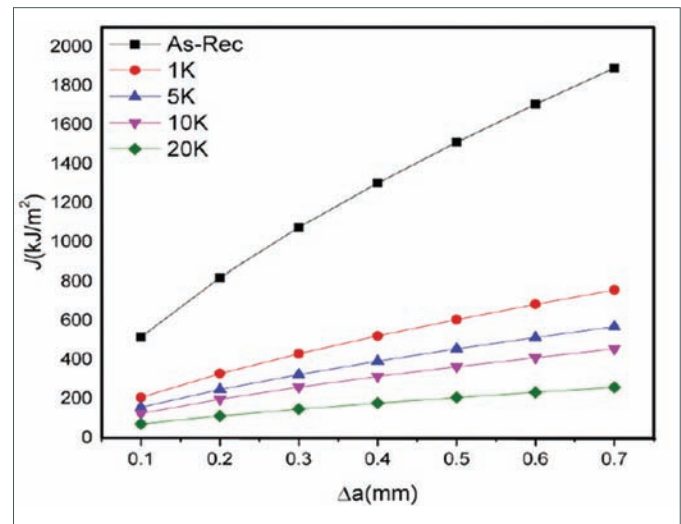


Figure 6: J-R curves for as-received and aged conditions of Alloy 617

$$J_{0.2t} = 11.44 * KV * (Ag)^{1/3} [((3.05 * KV) / R_m)^3 A_g + 0.2]^{(2/3)} \quad (5)$$

It has been estimated from the J-R curves shown in Figure 6, that there is a drastic reduction in fracture toughness from the as-received condition to the material aged for 1 kh. Further aging time results in progressive reduction of fracture toughness but to a much smaller degree. It is to be noted that the curve of the as-received material is very steep while all the aged conditions show much shallower J-R curves. J_0 , $J_{0.2}$ and $J_{0.2t}$ are given in Table 2. It can be seen that $J_{0.2}$ is the conservative value for as-received material while J_0 is conservative for all the aged conditions. Also, as can be made out from the J-R curve all the 3 measures of crack initiation J are within maximum allowable crack extension (peak load). Thus, the $J_{0.2}$ and J_0 obtained are valid for as-received and aged conditions respectively.

In summary, the Alloy 617 has been extensively studied for its application toward advanced ultra-supercritical thermal power plants. Microstructural and mechanical properties have been judiciously studied in compliance with various ASTM standards procedures. In the light of above, results and discussion, it is obvious that Alloy 617 is a promising candidate material towards next-generation thermal power plants.

Aditya Narayan Singh
Metallurgy and Materials Group

Forthcoming Meetings/Conferences

The Second Quadrennial International CONFERENCE on Structural Integrity (ICONS-2018) **December 14-17, 2018 @IITM Chennai**

Indira Gandhi Centre for Atomic Research (IGCAR), Kalpakkam and Society for Failure Analysis (SFA), Chennai Chapter together with other Indian Institutes such as IITM Chennai, IISc, Bangalore and InSIS, Bangalore are organizing the second quadrennial International Conference on Structural Integrity (ICONS-2018) at IITM Chennai during the period of December 14-17, 2018.

ICONS-2018 aims to bring together the multidisciplinary community of engineers, scientists, academicians, industry experts, plant managers and regulatory personnel to discuss the recent trends and future directions in structural integrity. The scope of the conference includes mainly fatigue and fracture mechanics of metals, composites, bio and nanomaterials, steel and concrete structures, mechanical behaviour of materials, experimental, computational and analytical methods in fatigue and fracture assessment, failure analysis, creep and creep-fatigue interaction, structural health and condition monitoring & non-destructive evaluation, in-service inspection, remote handling and robotics, fracture based design and analysis on structural integrity, remaining life assessment and extension, damage mechanics etc.

Address for Correspondence:

R. Suresh Kumar

Convener, Organising Committee, ICONS-2018

Head, High-Temperature Analysis Section

Reactor Design Group

Indira Gandhi Centre for Atomic Research (IGCAR)

Kalpakkam - 603102 (Tamil Nadu), INDIA

Tel:+91-44- 27480117, Fax: +91-44-27480068

Mobile: +91 9443881100

Email: icons2018con@gmail.com

Website: <http://web.iitm.ac.in/icons2018/>

Forthcoming Meetings/Conferences

11th National Conference on REcent ADvances in Information Technology (READIT 2018) August 8-9, 2018

Scientific Information Resource Division (SIRD), Indira Gandhi Centre for Atomic Research (IGCAR), Kalpakkam and Madras Library Association – Kalpakkam Chapter (MALA-KC) have been conducting a series of biennial national conferences on Recent Advances in Information Technology (READIT) since 1995. The earlier ten READIT conferences conducted were well received by professionals engaged in IT and Library Science from R&D and Academic Institutions from various parts of the country. It is now planned to conduct a two day READIT-2018 national conference with a theme of “Reinventing Libraries: Digital Innovations & Technologies” which include invited lectures by specialists from various parts of the country.

SCOPE

READIT provides a forum for discussion on information access and knowledge transfer in libraries. The objective of READIT-2018 is focused on how Technology can be applied in Library Services in line with the emerging trends.

Following are the broad areas included in the scope of the conference:

- Digital Innovations & Technologies in Libraries
- Personalization in Digital Library Services: Issues & Solutions
- Smart Libraries based on Cloud Computing & Internet of things
- Semantic Web Technology for Libraries
- Information Sharing in Consortia and Virtual Private Networks
- Metadata Creation Tools & User Centric Collection Building
- Enhancing the Information access in R&D Environment

Address for Correspondence

S. Rajeswari

Convener, Organizing Committee, READIT-2018

Head, Scientific Information Resource Division

Indira Gandhi Centre for Atomic Research

Kalpakkam – 603 102, Tamil Nadu

Phone: 044 27480281 / 044 27480500 extn 22387

e-mail: readit@igcar.gov.in

Website: <http://www.igcar.gov.in/seminars/readit2018/>

NEWS and Events



Delegation from IAEA / METI with Dr. Arun Kumar Bhaduri, Director, IGCAR and senior colleagues of the Centre

A delegation from IAEA / METI visited the Centre on January 8, 2018. The delegation visited the Fast Breeder Test Reactor, Sodium experimental facilities in FRTG and Metal Fuel Fabrication Facilities.



Prof. W. Arnold, Saarland University, Germany delivering the IGC colloquium

Prof. W. Arnold, Department of Material Science and Materials Technology, Saarland University, Germany delivered the IGC colloquium on the topic "Surface Mechanical Properties of Comet 67P" on February 13, 2018

Visit of Dignitaries



Dr. M. R. Srinivasan, Member, AEC along with Dr. Arun Kumar Bhaduri, Director, IGCAR and senior colleagues of the Centre

Dr. M. R. Srinivasan, Member, Atomic Energy Commission visited the Centre on March 6, 2018 and had discussions with senior colleagues. He also visited Shake Table and Fast Breeder Test Reactor Facilities



Visit of Shri Gopal Baglay, Joint Secretary, Prime Minister's Office

Shri Gopal Baglay Joint Secretary, Prime Minister's Office visited the Centre on March 17, 2018. He visited the Fast Breeder Test Reactor and KAMINI


HBNI-IGCAR Corner


Ph.D Thesis Defense


Name	Title	Date	Discipline
 <p>Shri D. Sanjay Kumar</p>	<p>Studies on Novel Methods of Synthesis and Sintering of Nanocrystalline Ceramics</p>	<p>10-01-2018</p>	<p>Chemical Sciences</p>
 <p>Ms. A. V. Meera</p>	<p>Thermochemical Investigations on Bi-Fe-O and Bi-Cr-O Systems</p>	<p>30-01-2018</p>	<p>Chemical Sciences</p>
 <p>Shri Sajal Ghosh</p>	<p>Thermochemical Studies of Alloys and Molten Halide Salts of Relevance to Pyrochemical Reprocessing of Metallic Fuel</p>	<p>16-03-2018</p>	<p>Chemical Sciences</p>
 <p>Shri S. Nagaraju</p>	<p>Effect of Welding Processes on the Weld Attributes of 9Cr-1Mo Steel Weld Joints</p>	<p>10-01-2018</p>	<p>Engineering Sciences</p>

Ph.D Thesis Defense			
Name	Title	Date	Discipline
 Shri Samba Siva Rao Kambala	Study on development of a Pulsed Eddy Current System for Testing Thick Stainless Steel Components	25-01.2018	Engineering Sciences
 Ms. S. Sravanthi	An Investigation into the Fail Safeness of Safety Critical Instrumentation & Control in a Sodium Cooled Fast Reactor	26-02-2018	Engineering Sciences
 Shri K. Srinivasan	Investigations on the Discrete Wigner Functions of Multi-Qubit Systems	06.03.2018	Physical Sciences
 Shri Barid Baran Lahiri	Studies on Hyperthermia in Magnetic Fluids: Effects of Particle Loading, Medium Viscosity, Size Polydispersity, Orientational Ordering and Thermal Losses on Heating Efficiency	22.03.2018	Physical Sciences

AWARDS

Ultrahigh Wear Resistance of Ultrananocrystalline Diamond Nanowall Thin Film

Revati Rani and Niranjana Kumar

"International Nanotribology Forum, NanoGoa: Nanoscale Effects in Macrotribology", held at Goa during January 8-12, 2018

Best Paper Award

Awards and Honours

Dr. John Philip has been selected as a Member of Editorial Board of Infrared Physics and Technology, Elsevier, Netherland.

Dr. John Philip has been selected as a Member of Research Council of CSIR-Central Glass & Ceramic Research Institute (CSIR-CGCRI), Kolkata.

Ms. Jemimah Ebenezer of Computer Division was conferred "Distinguished Women in Engineering" for her contribution and achievements in the field of Electronics Engineering at 3rd Annual Women's Meet-AWM 2018 conducted by Venus International Foundation, Chennai on March 3, 2018

Best Paper/Poster Award

A Comparative Study of the Diagnostic X-ray Attenuation Property of β -Bi₂O₃ and Bi Nanoparticles Based Nanocomposites

Ms J. Sangeetha, Shri T. Saravanan and Dr. John Philip

International Seminar on Advanced Nanomaterials- 2018 (ISAN-2018), held during February 27-28, 2018, National Centre for Nanoscience and Nanotechnology, University of Madras, Chennai

C. V. Raman Best Poster Award

Role of Field-Induced Nanostructures and Polydispersity on Effective Thermal Transport in Magnetic Fluids

Ms Sithara Vinod and Dr. John Philip

International Seminar on Advanced Nanomaterials- 2018 (ISAN-2018), held during February 27-28, 2018, National Centre for Nanoscience and Nanotechnology, University of Madras, Chennai

Best Paper Award

Evaluating the efficacy of PDMS Nanocomposites to Inhibit Barnacle Settlement: A Comparison of Laboratory and Field Assays

Shri S. Venkatnarayanan, Shri P. Sriyutha Murthy, Shri Arindam Das, Shri V. Pandiyan, Shri V. S. Sathyaseelan, Shri B. Anandkumar, Shri R. Kirubakaran and Shri V. P. Venugopalan

International Seminar on Advanced Nanomaterials - 2018 (ISAN- 2018) held during February 27-28, 2018, National Centre for Nanoscience and Nanotechnology, University of Madras, Chennai

C. V. Raman Best Poster Award

Oxidation and Corrosion behavior of Ni-based Amorphous Alloy in the Nitric Acid Environment

Shri Chiranjit Poddar, Shri J. Jayaraj and Dr. S. Ningshen

International Corrosion Prevention Symposium for Research Scholars, CORSYM-2018, March 23-24, 2018 IIT Madras, Chennai.

Best Paper Award

Optimization of CVD Silicon Carbide Interlayer for Plasma Sprayed Ytria on High Density Graphite for Pyrochemical Reprocessing

Shri B. Madhura, Shri E. Vetrivendan, Dr. Ch. Jagadeeswara Rao, Shri A. Udayakumar and Dr. S. Ningshen

International Corrosion Prevention Symposium for Research Scholars, CORSYM-2018, March 23-24, 2018, IIT Madras, Chennai

Best Paper Award

Biodiversity Basket - Avian Fauna



Asian Openbill

Asian Openbill is from Stork family. These are large in size and long-legged wader birds and commonly found in Kalpakkam

Editorial Committee Members: Dr. T. S. Lakshmi Narasimhan, Dr. N. V. Chandra Shekar, Dr. C. K. Mukhopadhyay, Dr. Vidya Sundararajan, Shri A. Suriyanarayanan, Dr. C. V. S. Brahmananda Rao, Dr. V. Subramanian, Ms. R. Preetha, Shri J. Kodandaraman, Shri G. Venkat Kishore, Shri S. Kishore, Dr. N. Desigan, Shri M. Rajendra Kumar, Shri V. Rajendran, Ms. S. Rajeswari, Shri K. Ganesan, Shri K. Varathan and Shri G. Pentaiah